Programmable Materials (2023), **Vol. 1**:e6 1–16
doi:10.1017/pma.2023.5

PROGRAMMABLE MATERIALS

RESEARCH ARTICLE

Architecting materials for extremal stiffness, yield, and buckling strength

Fengwen Wang and Ole Sigmund

Department of Civil and Mechanical Engineering, Technical University of Denmark, Lyngby, Denmark.

Corresponding author: Fengwen Wang; Email: fwan@dtu.dk

Received: 26 September 2022; **Revised:** 16 March 2023; **Accepted:** 6 April 2023

Keywords: architected material; stiffness; yield strength; buckling strength; topology optimisation

Abstract

This paper proposes a methodology for architecting microstructures with extremal stiffness, yield, and buckling strength using topology optimisation. The optimised microstructures reveal an interesting transition from simple lattice-like structures for yield-dominated situations to hierarchical lattice structures for buckling-dominated situations. The transition from simple to hierarchical is governed by the relative yield strength of the constituent base material as well as the volume fraction. The overall performances of the optimised microstructures indicate that maximum strength is determined by the buckling strength at low-volume fractions and yield strength at higher-volume fractions, regardless of the base material's relative yield strength. The non-normalised properties of the optimised microstructures show that higher base material Young's modulus leads to both higher Young's modulus and strength of the architected microstructures. Furthermore, the polynomial order of the maximum strength lines with respect to mass density obtained from the optimised microstructures reduces as base material relative yield strength decreases, reducing from 2.3 for buckling-dominated thermoplastic polyurethane to 1 for yield-dominated steel microstructures.

Contents

Introduction 1
Optimisation problem for 2D architected materials with enhanced stiffness and strength 3
Material stiffness and strength evaluations . . . 3
Design parameterisation . . . 5
Design problem formulation . . . 6
Results 7
Validation of the proposed approach . . . 8
Strength-optimised microstructure . . . 9
Optimised microstructures with tunable stiffness/yield and buckling strength . . . 10
Conclusions 14
References 15

Introduction

Exploring novel material architectures with extremal properties has been a constant quest in the field of material design and lightweight engineering. These developments have been further promoted by

advances in additive manufacturing facilitating fabrication of functional materials with unprecedented complexity (Meza et al., 2015; Zheng et al., 2016). As substitutions to trial and error and limited human intuition, topology optimisation methods have been shown to be powerful tools in designing novel materials in various applications (Sigmund, 2000; Bendsøe and Sigmund, 2003; Osanov and Guest, 2016). Up to now, however, the field of architected materials has focused on individual material properties-like stiffness, yield or buckling strength but less so on the intricate trade-off between these properties.

Material stiffness and strength are fundamental properties for determining material load-bearing capacity as they measure the material's deformation resistance and ultimate load-carrying capacity, respectively. The quest for optimal stiff and strong materials depends on many aspects, including the loading conditions and constituent base materials. Stiffness-optimal materials meeting theoretical upper bounds have been obtained via systematic design approaches (Sigmund, 1995; Guest and Prevost, 2006; Huang et al., 2011; Andreassen et al., 2014; Berger et al., 2017). It has been shown that plate microstructures reach the Hashin–Shtrikman bounds (Hashin, 1962) in the low-volume fraction limit and remain within 10% of the theoretical upper bounds at moderate volume fractions. A few studies have focused on improving microstructure strength, including stress minimisation and buckling strength optimisation. It has been shown that the maximum von Mises stress can be reduced when taking stress into account during the microstructure optimisation procedure either as constraints or objectives (Collet et al., 2018; Coelho et al., 2019; Alacoque et al., 2021; Ferrer et al., 2021). The stress singularity issue, where the stress at a point approaches infinity as the density at that point approaches zero, was handled by stress relaxation methods (Cheng and Guo, 1997; Duysinx and Bendsøe, 1998; Bruggi, 2008; Le et al., 2010). Large numbers of local stress constraints can be aggregated to a global quantity using the p-norm, Kresselmeier–Steinhauser (KS) (Kreisselmeier and Steinhauser, 1980) methods or by the augmented Lagrangian method (da Silva et al., 2021). Microstructure buckling strength optimisation using topology optimisation was first studied by Neves et al. (2002), focusing on cell-periodic buckling modes. More recently, 2D and 3D material microstructures were systematically designed to enhance buckling strength based on linear material analysis. This approach evaluates effective material properties using the homogenisation method (Hassani and Hinton, 1998) and material buckling strength under a given macro stress using linear buckling analysis (LBA) with Bloch–Floquet boundary conditions to capture all the possible buckling modes (Triantafyllidis and Schnaidt, 1993; Thomsen et al., 2018; Wang and Sigmund, 2021). Both studies showed that the optimised materials possess several times higher buckling strength than their references at the cost of some stiffness degradation. Subsequent 2D and 3D experimental verifications have further verified the buckling superiority of the optimised microstructures and validated the linear material evaluation (Bluhm et al., 2022; Wang et al., 2023).

So far, optimised microstructures have been designed considering material buckling or yield failure separately. However, yield-optimised microstructures tend to be vulnerable to buckling failure. On the other hand, buckling-optimised microstructures assume constituent base materials with relatively high yield strength (yield-strength-to-Young's-modulus ratio, σ_1/E_1), for example, elastomers. For other base materials with low relative yield strengths, for example, steel, the buckling-optimised microstructures fail due to localised yield. Hence, the optimised strength superiority in both cases may significantly degrade in real applications. Furthermore, a previous numerical study showed that for a given microstructure topology, the failure mechanism switches from buckling- to yield-dominated failure as the volume fraction increases (Andersen et al., 2021). Hence, it is crucial to consider both failure mechanisms in the design procedure considering different volume fractions. Furthermore, it is essential to provide microstructure candidates with programmable properties working for various base materials and volume fractions fitting various applications.

In this study, we extend the stiffness/buckling studies from Thomsen et al. (2018) and Wang and Sigmund (2021) to also include yield strength. Yield strength and Young's modulus share a monotonic relation in the optimised designs, as shown in the result section. Hence, microstructure will be designed systematically by maximising buckling strength with different yield strength bounds and considering

https://doi.org/10.1017/pma.2023.5 Published online by Cambridge University Press

different volume fractions. The optimised microstructure are further evaluated for different practical base materials ranging from low relative yield strength steel to high relative yield strength thermoplastic polyurethane (TPU).

The paper is organised as follows: Section 'Optimisation problem for 2D architected materials with enhanced stiffness and strength' summarises basic formulations to evaluate microstructure stiffness and strength, and formulates the optimisation problem for designing 2D microstructures with extremal properties. Section 'Results' validates the proposed approach and presents topology-optimised microstructure sets for different volume fractions and corresponding performances considering different base materials. Finally, Section 'Conclusions' concludes the study.

Optimisation problem for 2D architected materials with enhanced stiffness and strength

This section summarises the basic formulations for designing 2D architected materials with enhanced stiffness and strength using topology optimisation. The finite element method is combined with homogenisation theory and LBA to evaluate material properties (Cook et al., 2002). To accurately represent the stress situation, we employ the incompatible elements from Wilson et al. (1973) and Wilson and Ibrahimbegovic (1990), that is, the so-called Q_6 element. Two additional so-called incompatible modes are considered to represent bending deformations accurately. The reader is referred to the work by Wilson et al. (1973) and Wilson and Ibrahimbegovic (1990) for additional formulations for the Q_6 elements.

Material stiffness and strength evaluations

Under small strain assumptions, the material stiffness and strength are evaluated using the homogenisation approach and LBA together with Bloch–Floquet theory to account for buckling modes at different wavelengths based on the periodic microstructure. Figure 1 summarises the material stiffness and strength evaluation procedure.

The microstructure is assumed of unit size here. The symmetry properties of the effective elasticity matrix are exploited to represent the equations in a more compact form using the abbreviation $kl \rightarrow \alpha$: $11 \rightarrow 1$, $22 \rightarrow 2$, $(12, 21) \rightarrow 3$. The effective elasticity matrix is calculated by an equivalent energy-based homogenisation formulation (Sigmund, 1995; Hassani and Hinton, 1998) via

$$\begin{aligned} \bar{D}_{\alpha\beta} = \frac{1}{|Y|} \sum_{e=1}^{N} \int_{Y^e} \left(\tilde{\boldsymbol{\varepsilon}}_\alpha - \hat{\mathbf{B}}^e \boldsymbol{\chi}_\alpha^e \right)^T \mathbf{D}^e \left(\tilde{\boldsymbol{\varepsilon}}_\beta - \hat{\mathbf{B}}^e \boldsymbol{\chi}_\beta^e \right) dY, \\ \mathbf{K}_0 \boldsymbol{\chi}_\alpha = \mathbf{f}_\alpha, \quad \alpha = 1, 2, 3, \\ \boldsymbol{\chi}_\alpha|_{x=1} = \boldsymbol{\chi}_\alpha|_{x=0}, \quad \boldsymbol{\chi}_\alpha|_{y=1} = \boldsymbol{\chi}_\alpha|_{y=0}. \end{aligned} \tag{1}$$

Here, $|Y|$ denotes the volume of the microstructure, $\sum$ represents a finite element assembly operation over all N elements, the superscript $()^T$ denotes the transpose, $\hat{\mathbf{B}}^e$ with a size of 3×8 is the condensed strain-displacement matrix of element e in the Q_6 element formulation, $\mathbf{D}^e$ is the elasticity matrix of the material in element e, $\tilde{\boldsymbol{\varepsilon}}_\alpha = \left[\delta_{\alpha\beta}\right]$ denotes the three independent unit strain fields, $\mathbf{f}_\alpha$ is the condensed equivalent load vector induced by the αth unit strain, and $\mathbf{K}_0$ is the global condensed elastic stiffness matrix. The detailed formulation of $\mathbf{K}_0$ and $\mathbf{f}_\alpha$ can be found in Wilson and Ibrahimbegovic (1990) and Thomsen et al. (2018).

The effective material compliance matrix is $\bar{\mathbf{C}} = \bar{\mathbf{D}}^{-1}$. Under plane stress assumptions, the effective Young's and bulk moduli are calculated using the effective elasticity or compliance matrices, stated as

$$\bar{E} = \frac{1}{\bar{C}_{11}}, \quad \bar{\kappa} = \frac{\bar{D}_{11} + \bar{D}_{12}}{2}. \tag{2}$$

https://doi.org/10.1017/pma.2023.5 Published online by Cambridge University Press

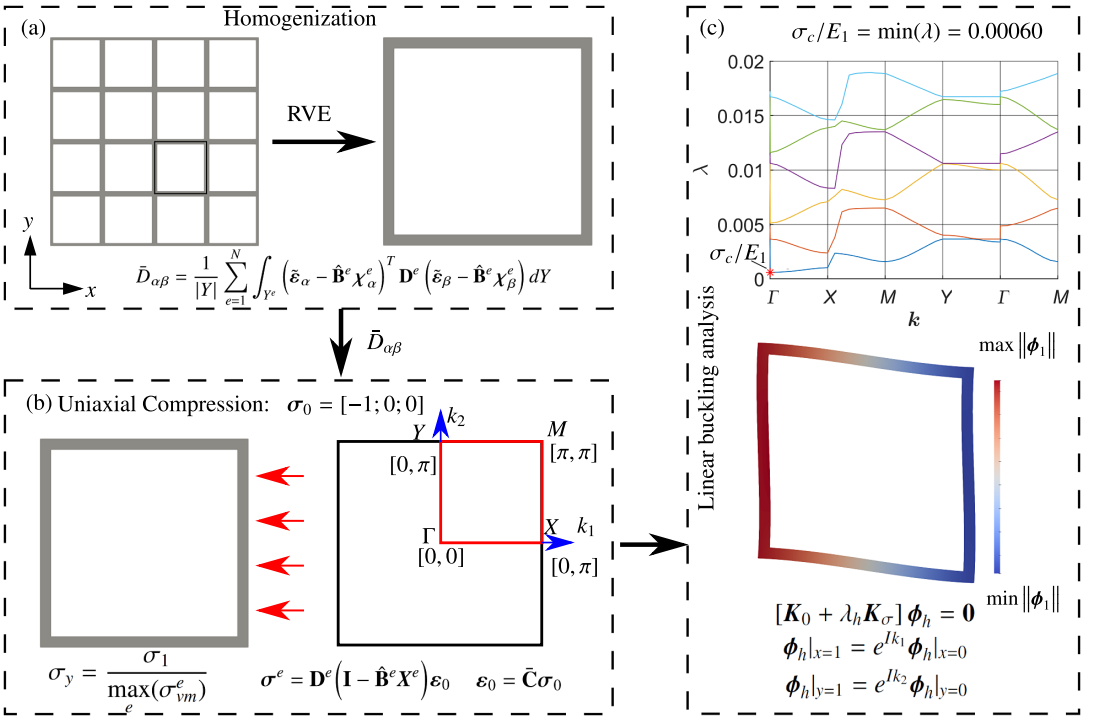

Figure 1. *Flowchart for material stiffness and strength evaluations based a stiffness-optimal orthotropic material with a volume fraction of 0.2. (a) Homogenisation of a periodic material using a representative volume element (RVE), that is, microstructure. (b) Calculation of yield strength and illustration of the corresponding irreducible Brillouin zone (IBZ) using uniaxial compression. (c) Buckling band structure, buckling strength, and mode.*

For a prescribed macroscopic stress state, $\boldsymbol{\sigma}_0$, the corresponding stress state of element e is obtained by the superposition of the three perturbation fields induced by the three unit strain fields in Eq. (1), expressed as

$$\boldsymbol{\sigma}^e = \mathbf{D}^e\left(\mathbf{I} - \hat{\mathbf{B}}^e\boldsymbol{X}^e\right)\boldsymbol{\varepsilon}_0, \text{ with } \boldsymbol{\varepsilon}_0 = \bar{\mathbf{C}}\boldsymbol{\sigma}_0, \tag{3}$$

where $\boldsymbol{\sigma}_0 = \boldsymbol{n}$ with $\boldsymbol{n}$ indicating the loading direction, $\boldsymbol{n} = [-1, 0, 0]^T$ for the uniaxial loading case, $\boldsymbol{X}^e = \left[\chi_1^e \ \chi_2^e \ \chi_3^e\right]$ is a 8×3 matrix containing the element perturbation fields.

The yield strength of the microstructure, σ_y, is determined by the ratio between the base material yield strength (σ_1) and the maximal von Mises stress in the microstructure, given as

$$\sigma_y = \frac{\sigma_1}{\max_e(\sigma_{vm}^e)}. \tag{4}$$

Here, σ_{vm}^e is the elemental von Mises stress, calculated by

$$\sigma_{vm}^e = \sqrt{\sigma_1^e\sigma_1^e - \sigma_1^e\sigma_2^e + \sigma_2^e\sigma_2^e + 3\sigma_3^e\sigma_3^e} = \sqrt{(\boldsymbol{\sigma}^e)^T\boldsymbol{M}\boldsymbol{\sigma}^e}, \tag{5}$$

where $\boldsymbol{M} = \begin{bmatrix} 1 & -1/2 & 0 \\ -1/2 & 1 & 0 \\ 0 & 0 & 3 \end{bmatrix}$.

https://doi.org/10.1017/pma.2023.5 Published online by Cambridge University Press

Based on the stress distribution in the microstructure, subsequent LBA is performed to evaluate the material buckling strength. Both short- and long-wavelength buckling is captured by employing the Floquet–Bloch boundary conditions in the LBA (Triantafyllidis and Schnaidt, 1993; Neves et al., 2002; Meza et al., 2017; Thomsen et al., 2018), stated as

$$\begin{aligned} [\boldsymbol{K}_0 + \lambda_h \boldsymbol{K}_\sigma]\, \boldsymbol{\phi}_h &= \boldsymbol{0}, \\ \boldsymbol{\phi}_h|_{x=1} = e^{Ik_1} \boldsymbol{\phi}_h|_{x=0}, \quad \boldsymbol{\phi}_h|_{y=1} &= e^{Ik_2} \boldsymbol{\phi}_h|_{y=0}. \end{aligned} \tag{6}$$

Here, $\boldsymbol{K}_\sigma = \sum_e \boldsymbol{K}_\sigma^e$ is the stress stiffness matrix with $\boldsymbol{K}_\sigma^e$ being the elemental stress stiffness matrix, $I = \sqrt{-1}$ is the imaginary unit, the smallest eigenvalue, λ_1, is the critical buckling strength for the given wave vector ($\boldsymbol{k} = [k_1, k_2]^T$), and $\boldsymbol{\phi}_1$ is the associated eigenvector.

The material buckling strength, σ_c, is determined by the smallest eigenvalue for all the possible wave vectors in Eq. (6), located in the first Brillouin zone, λ_{min}, that is, $\sigma_c = \min_{h,\boldsymbol{k}} \lambda_h$. The associated eigenvector is the critical buckling mode. The first Brillouin zone is the primitive cell in reciprocal space (Brillouin, 1953), spanning over $k_j \in [-\pi,\ \pi]$, $j = 1, 2$. Previous studies have shown that the critical buckling mode can be captured by sweeping $\boldsymbol{k}$-vectors along the boundaries of the irreducible Brillouin zone (IBZ) (Geymonat et al., 1993; Thomsen et al., 2018) that is determined by the shared symmetries between the microstructure geometry and the macroscopic stress state. In this study, we focus on designing a square cell in Figure 1(a) under uniaxial stress and the corresponding IBZs is illustrated in Figure 1(b). Figure 1(c) shows the corresponding buckling band diagrams calculated as customary along the boundaries of IBZ and critical buckling modes for the volume fraction of 20%. It is seen that buckling strength is determined by a global shear mode with $\sigma_c/E_1 = 0.00060$ with $\bar{E}/E_1 = 0.1074$. From the computational point of view, it is more convenient to perform LBA via $[-\tau_h \boldsymbol{K}_0 - \boldsymbol{K}_\sigma]\, \boldsymbol{\phi}_h = \boldsymbol{0}$, where $\tau_h = 1/\lambda_h$.

Design parameterisation

Based on the FEM discretisation, an element-wise constant physical design variable, $\bar{\rho}_e$, is employed to represent the material distribution in element e, with $\bar{\rho}_e = 1$ and $\bar{\rho}_e = 0$ representing base material and void, respectively. As in Thomsen et al. (2018), to suppress the spurious buckling modes associated with the low-stiffness elements, different interpolation schemes are employed for the elastic stiffness and stress stiffness using the solid isotropic material with penalisation (SIMP) model (Bendsøe and Sigmund, 1999). The ε-relaxed approach from Cheng and Guo (1997) is employed for the von Mises stress interpolation to avoid the stress singularity phenomenon. The interpolation schemes are written as

$$E_e = \begin{cases} \bar{\rho}_e^p (E_1 - E_0) + E_0, & \text{for } \boldsymbol{K}_0, \mathbf{f}_\alpha, \\ \bar{\rho}_e^p E_1, & \text{for } \boldsymbol{K}_\sigma, \\ \bar{\rho}_e / (\varepsilon(1 - \bar{\rho}_e) + \bar{\rho}_e)\, E_1, & \text{for } \sigma_{vm}^e. \end{cases} \tag{7}$$

Here, E_1 is the base material Young's modulus, $E_0 = 10^{-5} E_1$ represents void regions to avoid spurious modes located at the low-stiffness region, $p = 3$ is chosen as the standard penalisation factor. $\varepsilon = 0.002$ is chosen for the von Mises interpolation.

A hyperbolic tangent threshold projection is employed to generate physical design variables from the design variables, ρ_e, to enhance the discreteness of the optimised design (Wang et al., 2011). This is given as

$$\bar{\rho}_e = \frac{\tanh(\beta_1 \eta) + \tanh(\beta_1 (\widetilde{\rho}_e - \eta))}{\tanh(\beta_1 \eta) + \tanh(\beta_1 (1 - \eta))}, \tag{8}$$

where $\widetilde{\rho}_e$ is the filtered design variable calculated from the design variables, $\boldsymbol{\rho}$, using a PDE filter presented in Lazarov and Sigmund (2011). When β_1 is big, $\bar{\rho}_e \approx 1$ if $\widetilde{\rho}_e > \eta$ and $\bar{\rho}_e \approx 0$ if $\widetilde{\rho}_e < \eta$.

https://doi.org/10.1017/pma.2023.5 Published online by Cambridge University Press

Hence, the projection in Eq. (8) suppresses grey element density regions induced by the PDE filter, when β_1 is big and ensures black–white designs when the optimisation converges. Moreover, it mimics the manufacturing process, and is used in the robust design formulation context (Wang et al., 2011), where manufacturing errors are taken into accounts by choosing different thresholds, η. In this study, the maximum value of β is chosen to $\beta = 8$ allowing a small amount of grey regions in the design to avoid the mesh dependency of the maximum von Mises stress as discussed by da Silva et al. (2021).

Design problem formulation

The KS function (Kreisselmeier and Steinhauser, 1980) is employed to aggregate the elemental von Mises stress (σ^e_{vm}) to represent the maximum von Mises stress; to aggregate the considered eigenvalues for given $\boldsymbol{k}$-vectors ($\tau_h(\boldsymbol{k}_l)$); to represent the material buckling strength; or to aggregate both quantities to represent both yielding and buckling strength, stated as

$$KS\left(\kappa_1\sigma^e_{vm}/\sigma_1, \kappa_2\tau_h(\boldsymbol{k}_l)\right) = \frac{1}{\zeta}\ln\left(\kappa_1\sum_{e=1}^{N} e^{\zeta\,\sigma^e_{vm}/\sigma_1} + \kappa_2\sum_{l=1}^{n_h}\sum_{h=1}^{m_l} e^{\zeta\,(\tau_h(\boldsymbol{k}_l))}\right), \qquad \kappa_1, \kappa_2 \in \{0;1\}. \tag{9}$$

Here, $\kappa_1 = 1$ and $\kappa_2 = 0$ aggregate the elemental von Mises stress, $\kappa_1 = 0$ and $\kappa_2 = 1$ aggregate the eigenvalues for given $\boldsymbol{k}$-vectors, $\kappa_1 = 1$ and $\kappa_2 = 1$ to aggregate both quantities.

The optimisation problem for enhancing material stiffness and strength can be formulated to minimise a weighted value of the KS function in Eq. (9) and $\bar{E}^{-1}$, stated as

$$\begin{aligned}
\min_{\boldsymbol{\rho}} \quad & \left(\gamma_1 KS\left(\kappa_1\sigma^e_{vm}/\sigma_1, \kappa_2\tau_h(\boldsymbol{k}_l)\right) + (1-\gamma_1)\bar{E}^{-1}\right)E_1, \qquad \kappa_1, \kappa_2 \in \{0;1\},\\
s.t. \quad & \left[-\tau_h\boldsymbol{K}_0(\boldsymbol{k}_l) - \boldsymbol{K}_\sigma(\boldsymbol{k}_l)\right]\boldsymbol{\phi}_h = \mathbf{0},\\
& \mathbf{K}_0\boldsymbol{\chi}_\alpha = \mathbf{f}_\alpha, \quad \alpha = 1,2,3,\\
& KS\left(\sigma^e_{vm}/\sigma_1\right)E_1 \le 1/\sigma^*.\\
& \bar{E}/E_1 \ge E^*,\\
& f = \sum_e v_e\bar{\rho}_e \Big/ \sum_e v_e \le f^*,\\
& \mathbf{0} \le \boldsymbol{\rho} \le \mathbf{1}.
\end{aligned} \tag{10}$$

Here, γ_1 is the weight, $\gamma_1 = 0$ and $\gamma_1 = 1$ represent stiffness and strength optimisation, respectively. E_1 in the objective normalises the microstructure strength and stiffness with respect to the base material Young's modulus. σ^* is the normalised yield strength lower bound, E^* is the normalised Young's modulus lower bound, v_e is the volume of element e, and f and f^* are the actual and the prescribed upper bound of the volume fraction in the microstructure.

The sensitivity of a component, $\bar{D}_{\alpha\beta}$, in the effective elastic matrix $\bar{\boldsymbol{D}}$ with respect to $\bar{\rho}^e$, is written as

$$\frac{\partial\bar{D}_{\alpha\beta}}{\partial\bar{\rho}^e} = \frac{1}{|Y|}\int_{Y^e}\left(\tilde{\boldsymbol{\varepsilon}}_\alpha - \hat{\mathbf{B}}^e\boldsymbol{\chi}^e_\alpha\right)^T\frac{\partial\mathbf{D}^e}{\partial\bar{\rho}^e}\left(\tilde{\boldsymbol{\varepsilon}}_\beta - \hat{\mathbf{B}}^e\boldsymbol{\chi}^e_\beta\right). \tag{11}$$

The sensitivities of $\bar{E}$ can be analytical derived using Eqs. (2) and (11).

The sensitivities of elemental von Mises stress (σ^e_{vm}) with the respect to $\bar{\rho}^e$ is calculated using the adjoint sensitivity analysis by

$$\frac{\partial\sigma^e_{vm}}{\partial\bar{\rho}^e} = \frac{(\boldsymbol{\sigma}^e)^T\boldsymbol{M}}{\sqrt{(\boldsymbol{\sigma}^e)^T\boldsymbol{M}\boldsymbol{\sigma}^e}}\left[\frac{\partial\mathbf{D}^e}{\partial\bar{\rho}^e}\left(\mathbf{I} - \hat{\mathbf{B}}^e\boldsymbol{X}^e\right)\boldsymbol{\varepsilon}_0 + \mathbf{D}^e\left(\mathbf{I} - \hat{\mathbf{B}}^e\boldsymbol{X}^e\right)\frac{\partial\boldsymbol{\varepsilon}_0}{\partial\bar{\rho}^e}\right] + \sum_{\alpha=1}^{3}\left(\boldsymbol{\varphi}^e_\alpha\right)^T\left[\frac{\partial\boldsymbol{K}^e_0}{\partial\bar{\rho}^e}\boldsymbol{\chi}^e_\alpha - \frac{\partial\mathbf{f}^e_\alpha}{\partial\bar{\rho}^e}\right]. \tag{12}$$

https://doi.org/10.1017/pma.2023.5 Published online by Cambridge University Press

Here, $\partial \boldsymbol{\varepsilon}_0 / \partial \bar{\rho}^e$ can be directly derived using Eqs. (3) and (11), the adjoint vectors $\boldsymbol{\Phi} = \left[\boldsymbol{\varphi_1}, \boldsymbol{\varphi_2}, \boldsymbol{\varphi}_3\right]$ are obtained by solving

$$\boldsymbol{K}_0 \boldsymbol{\Phi} = \sum_e \left[\frac{(\boldsymbol{\sigma}^e)^T \boldsymbol{M}}{\sqrt{(\boldsymbol{\sigma}^e)^T \boldsymbol{M} \boldsymbol{\sigma}^e}} \mathbf{D}^e \hat{\mathbf{B}}^e \right]^T [\boldsymbol{\varepsilon}_0]^T . \tag{13}$$

Assuming that the eigenvector is normalised, as $(\boldsymbol{\phi}_h)^H \boldsymbol{K}_0 \boldsymbol{\phi}_h = 1$, the sensitivity of eigenvalue τ_h with respect to $\bar{\rho}^e$ can be obtained via the adjoint sensitivity analysis as described below (Thomsen et al., 2018),

$$\frac{\partial \tau_h}{\partial \bar{\rho}^e} = \left(\boldsymbol{\phi}_h^e\right)^H \left[-\tau_h \frac{\partial \boldsymbol{K}_0^e}{\partial \bar{\rho}^e} - \frac{\partial \boldsymbol{K}_\sigma^e}{\partial \bar{\rho}^e} \right] \boldsymbol{\phi}_h^e + (\boldsymbol{\phi}_h)^H \left[-\frac{\partial \boldsymbol{K}_\sigma}{\partial \boldsymbol{\varepsilon}_0} \frac{\partial \boldsymbol{\varepsilon}_0}{\partial \bar{\rho}^e} \right] \boldsymbol{\phi}_h + \sum_{\alpha=1}^{3} \left(\boldsymbol{\psi}_\alpha^e\right)^H \left[\frac{\partial \boldsymbol{K}_0^e}{\partial \bar{\rho}^e} \boldsymbol{\chi}_\alpha^e - \frac{\partial \mathbf{f}_\alpha^e}{\partial \bar{\rho}^e} \right]. \tag{14}$$

Here, $()^H$ denotes the complex conjugate, $\boldsymbol{\psi}_\alpha$ is the adjoint vector corresponding to $\boldsymbol{\chi}_\alpha$, which is obtained by

$$\boldsymbol{K}_0 \boldsymbol{\psi}_\alpha = \sum_e \left(\boldsymbol{\phi}_h^e\right)^H \left[\frac{\partial \boldsymbol{K}_\sigma^e}{\partial \boldsymbol{\chi}_\alpha^e} \right] \boldsymbol{\phi}_h^e. \tag{15}$$

The reader is referred to the work by Thomsen et al. (2018) for the detailed calculation of $\frac{\partial \boldsymbol{K}_\sigma^e}{\partial \boldsymbol{\chi}_\alpha^e}$. One of the advantages of using aggregation functions is the uniqueness of the gradient of eigenvalues, even when eigenvalues are repeated as stated by Torii and Faria (2017).

The sensitivities of the objective and constraints with respect to a design variable, ρ_e, are obtained using the chain rule. The optimisation problem is implemented in a flexible framework for large-scale topology optimisation (Aage et al., 2015) using the Portable Extensible Toolkit for Scientific computation (PETSc; Balay et al., 2016) and Scalable Library for Eigenvalue Problem Computations (SLEPc; Hernandez et al., 2005). The design is iteratively updated using the Method of Moving Asymptotes (MMA; Svanberg, 1987) based on the gradients of the objective and constraints. One case robust formulation in Wang and Sigmund (2021) is employed in this study, where the objective, yield, and stiffness constrains are evaluated on an eroded microstructure generated using $0.5 + \Delta\eta$ with the volume constraint working on the dilated microstructure generated with a threshold of $0.5 - \Delta\eta$. The volume constraint is updated every 20 iterations such that the volume constraint of the intermediate microstructure of $\eta = 0.5$ is satisfied. In this study, we choose $\Delta\eta = 0.05$.

Results

The proposed optimisation formulation is employed to design 2D square microstructures with 45°-symmetry to achieve tunable stiffness and buckling strength response while considering three different volume fractions, that is, $f^* = 0.2, 0.1, 0.05$. The unit cell is discretised by 512×512 Q_6 elements for $f^* = 0.2$ and the resolution is doubled in order to enable the evolution of structural hierarchy for $f^* = 0.1$ and $f^* = 0.05$. The filter radius is chosen to $r = 0.03$ for $f^* = 0.2$ and it is reduced to $r = 0.01$ for the two lower-volume fractions. A square cell with 45°-symmetry is designed. The initial microstructures (starting guesses) are chosen as the Young's modulus optimal microstructures with the prescribed volume fractions as shown in Figure 1. The presented designs are the blueprints with $\eta = 0.5$ unless otherwise stated. Smooth and sharp boundaries are extracted as contour lines from the optimised greyscale designs using the in-house code mentioned above, and subsequently evaluated in COMSOL using body-fitted meshes. The considered based material in the optimisation is pyrolytic carbon (PC) with a Poisson's ratio of $\nu = 1/3$ and a relative yield strength of $\sigma_1 / E_1 = 0.044$ (Crook et al., 2020).

https://doi.org/10.1017/pma.2023.5 Published online by Cambridge University Press

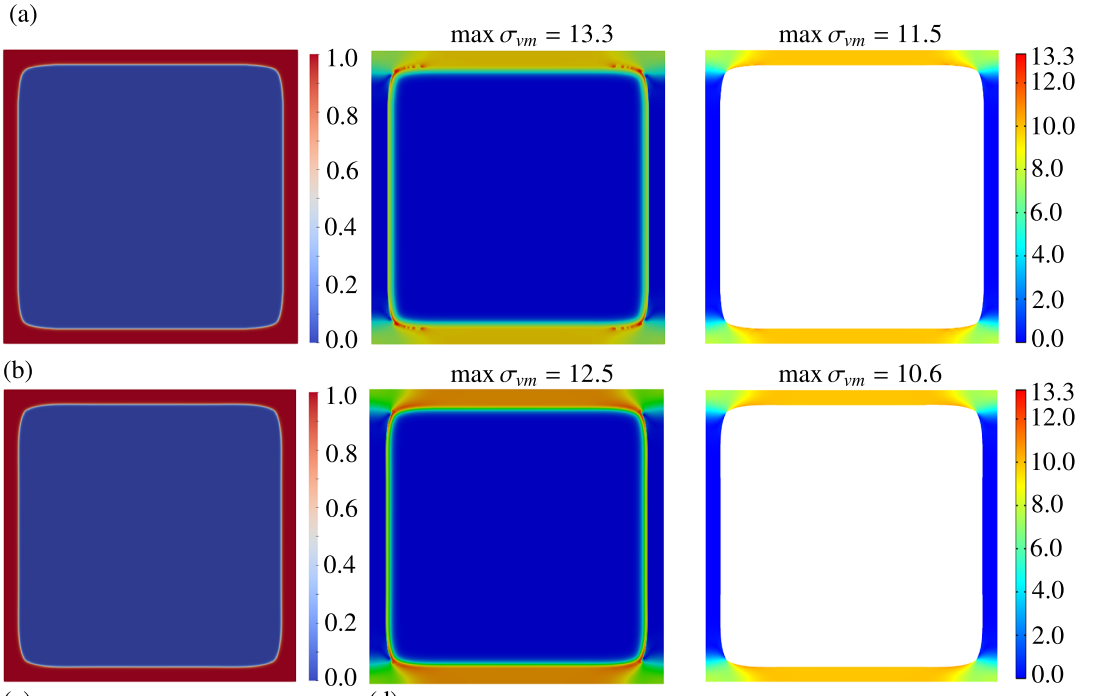

Design	(a) without σ^*	(b) with σ^*
Volume fraction	0.2	0.2
Greyness in-house (%)	2.6	2.6
$\bar{E}/E_1$ in-house	0.1035	0.1035
$\bar{E}/E_1$ COMSOL	0.1092	0.1092
σ_y/E_1 COMSOL	0.00382	0.00415
σ_c/E_1 COMSOL	0.00075	0.00075

Figure 2. *Optimised microstructures with maximised Young's modulus without (a) and with a yield strength constraint (b). Left: Optimised microstructures; Middle: von Mises stress distribution evaluated at the element centre using the in-house code with the optimised greyscale designs; Right: von Mises stress distribution evaluated using the extracted designs in COMSOL with body-fitted meshes. (c) Differences between the optimised designs. (d) Performance summary of the two designs.*

Validation of the proposed approach

In the first case, we maximise microstructure Young's modulus without or with the yield strength constraint by setting $\gamma_1 = 0$. The corresponding normalised yield strength lower bound is set $\sigma^* = 1/400$. The optimised designs are extracted using the 0.5 isocontour and imported into COMSOL for post-evaluation using second-order body-fitted meshes. Figure 2(a,b) presents the optimised microstructures obtained without and with the yield constraint, respectively. The left panels show the optimised microstructures, whereas the middle and right panels present the von Mises stress distribution evaluated using the in-house code and COMSOL. Both in-house code and COMSOL predict similar von Mises profiles and the same high von Mises stress regions. The intermediate physical densities in the optimised designs in the in-house code make the microstructure's perform slightly weaker (that is,

https://doi.org/10.1017/pma.2023.5 Published online by Cambridge University Press

lower effective Young's modulus) than the ones from COMSOL. Hence, the microstructures undergo bigger pre-strain as indicated by Eq. (3) and exhibit larger maximum von Mises stress compared to the post-evaluation in COMSOL. These conclusions are verified by the von Mises stress distributions in both designs shown in Figure 2(a,b).

The rather insignificant difference between the two designs is presented in Figure 2(c) using the 0.5 isocontours of the 1/8 cell at the upper right corner. The optimised microstructures possess very similar shapes with small deviations at the inner corner. The inner corner in the optimised microstructure with the yield constraint exhibits slightly lower curvatures to fulfil the yield strength constraint. The properties of the optimised microstructures evaluated from the in-house code and COMSOL are summarised in Figure 2(d). In the post-evaluation, both designs possess the same Young's modulus with 2% to the theoretical Young's modulus upper bound, $E_{HS} = f/(2-f)E_1$. The material buckling evaluations of both designs show that global shear modes dominate buckling failure, and both designs possess higher buckling strength than the initial design in Figure 1. The buckling strength enhancement is attributed to the round inner corner that makes the effect length of the member shorter than the initial design. Comparison between yield and buckling strengths shows that optimised microstructures fail due to yield.

The microstructure is subsequently optimised by maximising buckling strength with the same yield strength constraint, which results in the same topology due to the limited design freedom provided by the yield strength bound.

In the rest of the paper, all the designs and corresponding performance will be presented using the well-defined post-evaluation in COMSOL, unless otherwise stated.

Strength-optimised microstructure

In the second case, a microstructure is optimised to maximise the material strength, that is, maximising the minimum value between the buckling and yield strengths by choosing $\kappa_1 = 1$, $\kappa_2 = 1$, and $\gamma_1 = 1$. Figure 3 presents the optimised design and corresponding performance. Figure 3(a) shows the optimised 2×2 cells where the red box highlights the optimised microstructure. Figure 3(b,c) presents the corresponding critical buckling mode and von Mises stress distribution with titles showing the corresponding buckling and yield strengths. As in the previous designs, the critical buckling mode is a global shear mode. Compared to them, the optimised design develops hierarchy to enhance the microstructure buckling strength. The hierarchy in the design enhances the effective width-to-length ratio of the members and leads to a higher buckling strength. On the other hand, it reduces

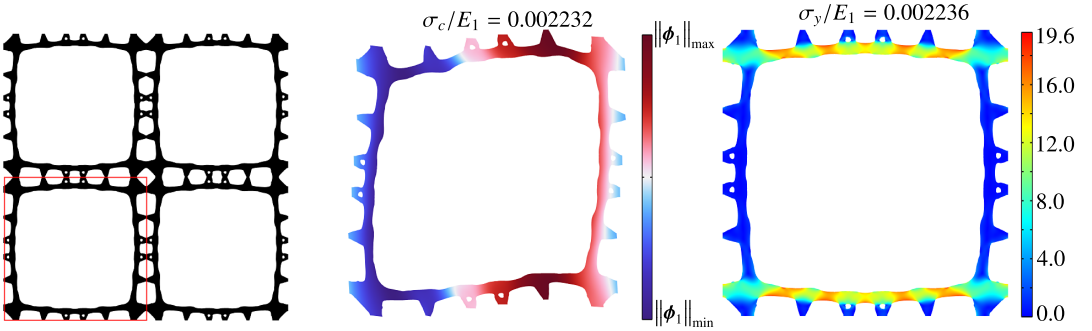

Figure 3. *Optimised microstructure with maximised material strength. (a) 2×2 optimised cells, the red region highlights the optimised microstructure. (b) Buckling failure mode with title representing buckling strength. (c) von Mises stress distribution under uniaxial compression with title representing the yield strength.*

https://doi.org/10.1017/pma.2023.5 Published online by Cambridge University Press

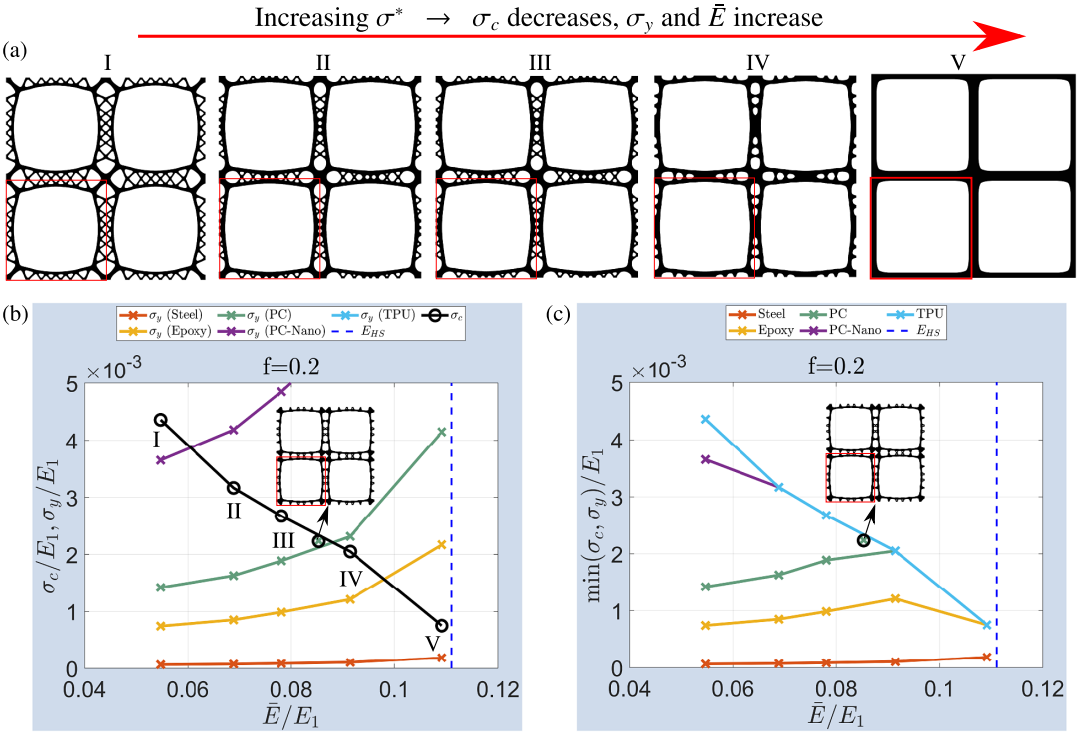

Figure 4. *Optimised microstructures for $f^* = 0.2$. (a) Optimised microstructures with increased yield strength bounds from left to right. (b) Yield/buckling strength versus Young's modulus performances for different constituent base materials. Black line with circles: Buckling strength versus Young's modulus curve. The other coloured lines: Yield strength versus Young's modulus. Aqua: TPU; purple: PC-Nano; teal: PC; yellow: epoxy; red: steel. (c) Strength versus Young's modulus performances.*

member stiffness and leads to a lower effective Young's modulus and yield strength. The optimised microstructure exhibits an effective Young's modulus of $\bar{E}/E_1 = 0.08533$, which is 21.9% degradation compared to the stiffness-optimal design. For the considered base material, PC, the corresponding buckling and yield strengths manifest that the optimised microstructure fails simultaneously due to buckling and yield failures.

Optimised microstructures with tunable stiffness/yield and buckling strength

We optimise microstructure sets by maximising material buckling strength with different yield strength bounds for different volume fractions by choosing $\kappa_1 = 0$, $\kappa_2 = 1$, and $\gamma_1 = 1$. The optimised design set for $f^* = 0.2$ is presented in Figure 4(a). As the required yield strength increases, the optimised microstructure becomes less hierarchical and converges to the stiffness/yield-strength-optimal one as shown in Figure 2(b) for a large yield strength constraint. The optimised microstructures' performance is evaluated using different base materials ranging from low relative yield strength steel to high relative yield strength TPU. Table 1 summarises the considered base materials and corresponding properties, including Young's modulus E_1, density ρ_1, and relative yield strengths, that is, the yield-strength-to-Young's-modulus ratio σ_1/E_1.

Figure 4(b) shows the normalised buckling strength (σ_c, black line with circles) and yield strengths for the considered base materials (σ_y, coloured lines with crosses, each colour represents one base material) versus Young's modulus performance. Figure 4(c) presents the optimised microstructures'

https://doi.org/10.1017/pma.2023.5 Published online by Cambridge University Press

Table 1. *Considered constituent base materials and corresponding properties (Crook et al., 2020; Andersen et al., 2021)*

	E_1 (GPa)	ρ_1 (kg/m^3)	σ_1/E_1
Steel	215	7,800	0.002
Epoxy	3.08	1,400	0.023
Pyrolytic carbon (PC)	62	1,400	0.044
Pyrolytic carbon-nano (PC-Nano)	350	2,600	0.113
Thermoplastic polyurethane (TPU)	0.012	1,190	0.333

strength versus Young's modulus performance. For the considered base material in the optimisation, that is, PC, represented by the teal lines, it is seen that the increase of the yield strength bound leads to optimised microstructures with increased yield strength and Young's modulus and reduced buckling strengths. The monotonic relation between the effective Young's modulus and yield strength is observed in the microstructure set. It is explained by Eq. (3) that the higher effective Young's modulus leads to a lower equivalent global strain for a given stress situation hence resulting in higher yield strength. For PC, the optimised design for material strength predicted by the optimised microstructure set is represented by the intersection between the buckling (the teal line with crosses) and yield strength (the black line with circles) curves. It is seen from Figure 4(b) that the strength-optimised design in Figure 3 possesses a material strength very close to the intersection point between the buckling curve (black) and the yield curve (teal), hence, it provides the best combined yield and buckling strength for PC.

The yield strength of the optimisation set for TPU represented by the aqua-coloured line is much bigger than the covered strength range in the plot; hence, it does not appear in Figure 4(b). For TPU, all the optimised designs are dominated by buckling failure due to its high relative yield strength, and all the optimised designs are dominated by yield failure for steel due to its low relative yield strength. Failure mechanism transition between yield and buckling is observed for the rest of the considered base materials. As the base material's relative yield strength increases, the transition between yield-dominated to buckling-dominated failure shifts to the left, that is, to lower Young's modulus microstructures. The strength-optimal microstructure switches to the optimised microstructure with a lower Young's modulus as the relative yield strength of the base material increases as seen in Figure 4(c).

To further explore the optimised microstructure failure at the lower-volume fractions, the microstructures are optimised for $f^* = 0.1$ and $f^* = 0.05$ by maximising microstructure buckling strength for different yield strength bounds.

Figure 5 presents the optimised microstructure set for $f^* = 0.1$ with increased yield strength bounds and the corresponding performances for different based materials. The geometrical evolutions in the design set show that the hierarchy vanishes as the required yield strength bound increases and the optimised microstructure configuration converges to the stiffness-optimal one for the largest yield strength bound. This observation is the same as in the previous case.

Unlike the previous case, the optimised microstructure set fails due to buckling for PC-Nano and TPU. The failure mechanism transits from the yield-dominated to the buckling-dominated failure for the rest of the base materials when the optimised microstructure evolves from the buckling-optimal microstructure at the left to the stiffness/yield-optimal one at the right in Figure 5(a) . Compared to the design set for $f^* = 0.2$, the transition point shifts further to a lower Young's modulus range with more hierarchy for $f^* = 0.1$ for the same base material.

Figure 6 summarises the optimised microstructure set for $f^* = 0.05$ and corresponding performances with different base materials. A similar geometrical evolution is observed as in the previous two design sets. The optimised microstructure set fails due to buckling failure for PC, PC-Nano, and TPU. Only

https://doi.org/10.1017/pma.2023.5 Published online by Cambridge University Press

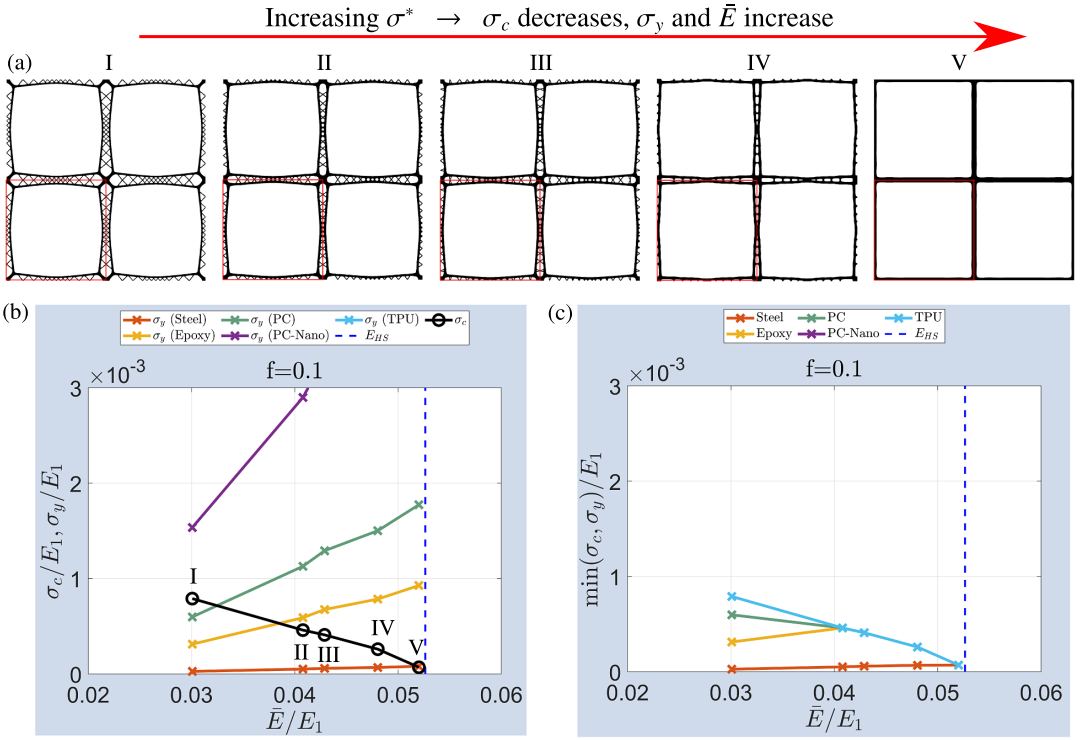

Figure 5. *Optimised microstructures for $f^* = 0.1$. (a) Optimised microstructures with increased yield strength bound from left to right. (b) Buckling/yield strength versus Young's modulus performance considering different base materials. (c) Microstructure strength versus Young's modulus performances.*

the buckling-optimised design with the lowest yield strength bound fails due to yield strength for epoxy, and the rest designs fail due to buckling. The failure mechanism transition is observed for steel. However, buckling failure dominates only the stiffness-optimal design, whereas yield failure dominates the rest designs. Compared with the previous two design sets for higher-volume fractions, the transition between yield- and buckling-dominated failure shifts further towards the buckling-optimised designs.

The overall comparison between the three microstructure sets shows that the optimised microstructures are mainly dominated by buckling failure for the low-volume fraction region, and they are dominated by yield failure for the high-volume fraction region. It can be expected that all the optimised designs, from the buckling-optimal design to the stiffness/yield-optimal design, fail only due to buckling at an even lower-volume fraction, and all the optimised designs have yield failure at much higher-volume fractions. The low critical volume fraction is determined when the full hierarchical buckling optimal microstructure fails due to buckling. The high critical volume fraction is determined when the corresponding stiffness-optimal microstructure exhibits yield failure. The critical volume fractions are determined by the relative yield strength of the base material. For a higher relative yield strength, the critical low-volume fraction is higher than the one with a lower one, whereas the high critical volume fraction is also higher.

To provide additional insight into the role of the choice of different base materials, Figure 7 summarises the non-normalised material properties versus mass density for the optimised microstructures. PC-Nano possesses the highest Young's modulus and high relative yield strength (see Table 1), hence, the optimised microstructures using PC-Nano exhibit the highest effective Young's modulus and strength while TPU results in the lowest effective Young's modulus and strength due to its low Young's

https://doi.org/10.1017/pma.2023.5 Published online by Cambridge University Press

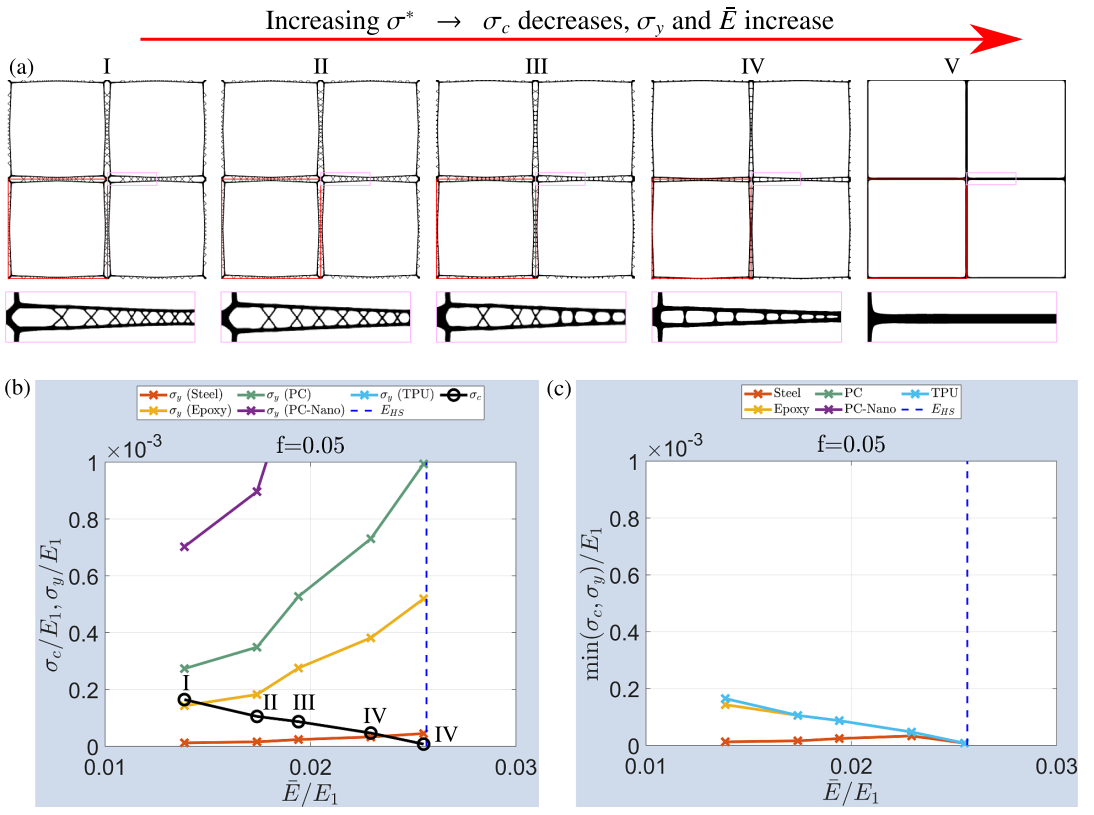

Figure 6. *Optimised microstructures for $f^* = 0.05$. (a) Optimised microstructures with increased yield strength bound from left to right. Pink boxes highlight the regions for enlarged views at the bottom. (b) Buckling/yield strength versus Young's modulus performances considering different base materials. (c) Microstructure strength versus Young's modulus performances.*

modulus. As expected, the maximum Young's modulus curve of the optimised microstructures matches the Hashin–Shtrikman bound, $E_{HS} = f/(2-f)E_1 = \rho/(2\rho_1 - \rho)E_1$; see the left panel.

The right panel presents the microstructure strength versus mass density, where ×'s indicate microstructures failed due to buckling, whereas ▲'s indicate microstructures failed due to yield. The dashed lines represent the maximum strength obtained from the optimised microstructures. By assuming a strength–mass–density relation of $\min(\sigma_c, \sigma_y) = c_0 f^{n_0} = c_0 \left(\frac{\rho}{\rho_1}\right)^{n_0}$, the order n_0 is obtained using the two points with lower densities and the orders for the different base materials are indicated in the strength plot as the line slopes. At low mass densities, the analytical yield strength upper bound follows the same relation as Young's modulus, that is, $\sigma_y = f/(2-f)\sigma_1 = \rho/(2\rho_1 - \rho)\sigma_1$, represented by the solid lines in the plot and it possesses a linear relation with respect to mass density with $n_0 = 1$. The minimum strength for TPU is controlled by the simple Young's modulus-optimal microstructures with first-order hierarchy (zeroth order indicates base material properties according to Lakes (1993)) and shows a close to cubic mass density dependency (Haghpanah et al., 2014). The maximum strength line for TPU is controlled by the optimised microstructures with second-order hierarchy, and it has a polynomial order of $n_0 = 2.3$ that is slightly lower than the predicted one, 2.5, assuming self-hierarchy (see Andersen et al., 2021), moreover with a higher coefficient c_0. As the relative yield strengths of the base materials decrease, the mass density dependency order reduces and converges to $n_0 = 1$ for steel that is governed by the yield upper bound. The maximum strength line meets the yield strength upper

https://doi.org/10.1017/pma.2023.5 Published online by Cambridge University Press

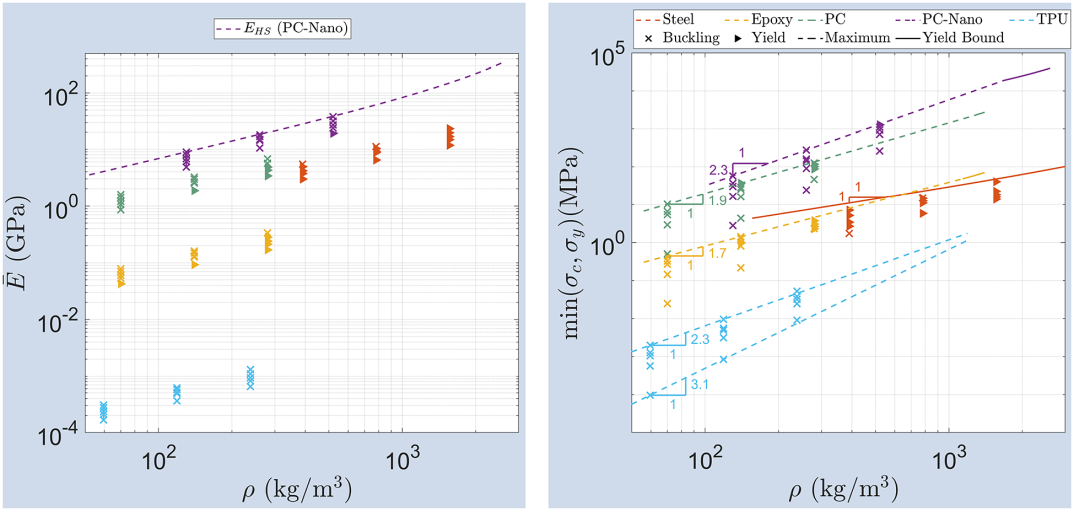

Figure 7. *Non-normalised properties of the optimised microstructures. Left: Young's modulus versus mass density with the dashed curve showing the Hashin–Shtrikman bound. Right: Strength versus mass density. The slopes indicate the polynomial order of the maximum strength lines to mass density.*

bound at relatively high mass density for epoxy, PC, and PC-Nano, while the one for TPU is solely governed by the maximum strength line, and the one for steel solely governed by the yield bound.

Conclusions

A general topology optimisation formulation is proposed to tailor microstructure properties, including stiffness, yield, and buckling strength. The formulation is validated by designing square cell microstructures with maximal stiffness and/or strength. Numerical results for stiffness-optimal microstructures show that yield strength can be enhanced by a yield strength constraint without sacrificing the material stiffness and buckling strength. Compared to the stiffness-optimised microstructures, strength-optimised microstructures develop geometric hierarchy that enhances their buckling resistance. These strength-optimised microstructures have considerably higher strengths and fail simultaneously due to yield and buckling at a slight decrease in stiffness.

Microstructure sets with volume fractions of 20%, 10%, and 5% are systematically designed by maximising buckling strength with different yield strength bounds. The geometric evolution of the optimised designs show that a lower yield strength bound allows microstructures to develop geometrical hierarchies, leading to higher buckling strength with decreased stiffnesses. Moreover, the effective Young's modulus and yield strength evolutions show a monotonic relation. The optimised microstructures are post-evaluated for base materials with different relative yield strengths ranging from steel to TPU. The overall performances show that base materials with higher relative yield strength allow the strength-optimal designs to form geometrical hierarchies, leading to higher optimised strength with slightly decreased Young's modulus. Furthermore, as the design volume fraction decreases, the transition between yield- to buckling-dominated failures moves further towards the buckling-optimised designs. The overall performance indicates that buckling strength determines optimised strength at low-volume fractions and yield strength at high-volume fractions. The base material's relative yield strength determines the critical volume fractions for pure buckling-dominated or pure yield-dominated failures. For a volume fraction in between, the strength-optimised microstructure is the optimised one with simultaneous yield and buckling failures. Meanwhile, the failure mechanism switches from yield- to buckling-dominated when the optimised microstructure configurations evolve

https://doi.org/10.1017/pma.2023.5 Published online by Cambridge University Press

from the buckling-strength to the stiffness/yield-strength optimised one. The non-normalised properties of the optimised microstructures show that base materials with higher Young's modulus lead to both higher Young's modulus and strength. The polynomial order of the maximum strength lines of the optimised microstructures on the mass density reduces as the base material relative yield strength decreases, reducing from 2.3 for TPU with buckling dominated to 1 for steel with yield dominated.

Data availability statement. The data that support the findings of this study are available from the corresponding author upon reasonable request.

Funding statement. This study was funded by the Villum Fonden through the Villum Investigator Project InnoTop.

Competing interest. The authors declare no competing interests exist.

Authorship contribution. F.W. designed and conducted the study, analysed the data, and wrote and edited the article. O.S. acquired funding, designed the study, analysed the data, and edited the article.

References

Aage N, **Andreassen E** and **Lazarov BS** (2015) Topology optimization using PETSc: An easy-to-use, fully parallel, open source topology optimization framework. *Structural and Multidisciplinary Optimization* **51**(3), 565–572.

Alacoque L, **Watkins RT** and **Tamijani AY** (2021) Stress-based and robust topology optimization for thermoelastic multi-material periodic microstructures. *Computer Methods in Applied Mechanics and Engineering* **379**, 113749.

Andersen MN, **Wang F** and **Sigmund O** (2021) On the competition for ultimately stiff and strong architected materials. *Materials & Design* **198**, 109356.

Andreassen E, **Lazarov B** and **Sigmund O** (2014) Design of manufacturable 3D extremal elastic microstructure. *Mechanics of Materials* **69**(1), 1–10.

Balay S, **Abhyankar S**, **Adams MF**, **Brown J**, **Brune P**, **Buschelman K**, **Dalcin L**, **Eijkhout V**, **Gropp WD**, **Kaushik D**, **Knepley MG**, **McInnes LC**, **Rupp K**, **Smith BF**, **Zampini S**, **Zhang H** and **Zhang H** (2016) PETSc users manual: Technical Report ANL-95/11 - Revision 3.7.

Bendsøe MP and **Sigmund O** (1999) Material interpolation schemes in topology optimization. *Archive of Applied Mechanics* **69**(9–10), 635–654.

Bendsøe MP and **Sigmund O** (2003) *Topology Optimization: Theory, Methods and Applications*. Berlin: Springer.

Berger J, **Wadley H** and **McMeeking R** (2017) Mechanical metamaterials at the theoretical limit of isotropic elastic stiffness. *Nature* **543**(7646), 533.

Bluhm GL, **Christensen K**, **Poulios K**, **Sigmund O** and **Wang F** (2022) Experimental verification of a novel hierarchical lattice material with superior buckling strength. *APL Materials* **10**(9), 090701.

Brillouin L (1953) *Wave Propagation in Periodic Structures: Electric Filters and Crystal Lattices*. New York: Dover.

Bruggi M (2008) On an alternative approach to stress constraints relaxation in topology optimization. *Structural and Multidisciplinary Optimization* **36**(2), 125–141.

Cheng GD and **Guo X** (1997) ε-relaxed approach in structural topology optimization. *Structural Optimization* **13**(4), 258–266.

Coelho PG, **Guedes JM** and **Cardoso JB** (2019) Topology optimization of cellular materials with periodic microstructure under stress constraints. *Structural and Multidisciplinary Optimization* **59**(2), 633–645.

Collet M, **Noël L**, **Bruggi M** and **Duysinx P** (2018) Topology optimization for microstructural design under stress constraints. *Structural and Multidisciplinary Optimization* **58**(6), 2677–2695.

Cook R, **Malkus D** and **Plesha M** (2002) *Concepts and Applications of Finite Element Analysis*. New York: Wiley.

Crook C, **Bauer J**, **Guell Izard A**, **Santos de Oliveira C**, **Martins de Souzae Silva J**, **Berger JB** and **Valdevit L** (2020) Plate-nanolattices at the theoretical limit of stiffness and strength. *Nature Communications* **11**(1), 1–11.

da Silva G, **Aage N**, **Beck A** and **Sigmund O** (2021) Local versus global stress constraint strategies in topology optimization: A comparative study. *International Journal for Numerical Methods in Engineering* **122**(21), 6003–6036.

Duysinx P and **Bendsøe MP** (1998) Topology optimization of continuum structures with local stress constraints. *International Journal for Numerical Methods in Engineering* **43**(8), 1453–1478.

Ferrer A, **Geoffroy-Donders P** and **Allaire G** (2021) Stress minimization for lattice structures. Part i: Micro-structure design. *Philosophical Transactions of the Royal Society A*, **379**(2201), 20200109.

Geymonat G, **Müller S** and **Triantafyllidis N** (1993) Homogenization of nonlinearly elastic materials, microscopic bifurcation and macroscopic loss of rank-one convexity. *Archive for Rational Mechanics and Analysis* **122**(3), 231–290.

Guest JK and **Prevost JH** (2006) Optimizing multifunctional materials: Design of microstructures for maximized stiffness and fluid permeability. *International Journal of Solids and Structures* **43**(22–23), 7028–7047.

Haghpanah B, **Papadopoulos J**, **Mousanezhad D**, **Nayeb-Hashemi H** and **Vaziri A** (2014) Buckling of regular, chiral and hierarchical honeycombs under a general macroscopic stress state. *Proceedings of the Royal Society A* **470**(2167), 20130856.

Hashin Z (1962) The elastic moduli of heterogeneous materials. *Journal of Applied Mechanics* **29**(1), 143–150.

https://doi.org/10.1017/pma.2023.5 Published online by Cambridge University Press

Hassani B and **Hinton E** (1998) A review of homogenization and topology optimization I - homogenization theory for media with periodic structure. *Computers & Structures* **69**(6), 707–717.

Hernandez V, **Roman JE** and **Vidal V** (2005) SLEPc: A scalable and flexible toolkit for the solution of eigenvalue problems. *ACM Transactions on Mathematical Software (TOMS)* **31**(3), 351–362.

Huang X, **Radman A** and **Xie YM** (2011) Topological design of microstructures of cellular materials for maximum bulk or shear modulus. *Computational Materials Science* **50**(6), 1861–1870.

Kreisselmeier G and **Steinhauser R** (1980) Systematic control design by optimizing a vector performance index. *IFAC Proceedings Volumes* **12**, 113–117.

Lakes R (1993) Materials with structural hierarchy. *Nature* **361**(6412), 511–515.

Lazarov BS and **Sigmund O** (2011) Filters in topology optimization based on Helmholtz-type differential equations. *International Journal for Numerical Methods in Engineering* **86**(6), 765–781.

Le C, **Norato J**, **Bruns T**, **Ha C** and **Tortorelli D** (2010) Stress-based topology optimization for continua. *Structural and Multidisciplinary Optimization* **41**(4), 605–620.

Meza L, **Zelhofer AJ**, **Clarke N**, **Mateos AJ**, **Kochmann D** and **Greer J** (2015) Resilient 3D hierarchical architected metamaterials. *Proceedings of the National Academy of Sciences of the United States of America* **112**(37), 11502–11507.

Meza LR, **Phlipot GP**, **Portela CM**, **Maggi A**, **Montemayor LC**, **Comella A**, **Kochmann DM** and **Greer JR** (2017) Reexamining the mechanical property space of three-dimensional lattice architectures. *Acta Materialia* **140**, 424–432.

Neves MM, **Sigmund O** and **Bendsøe MP** (2002) Topology optimization of periodic microstructures with a penalization of highly localized buckling modes. *International Journal for Numerical Methods in Engineering* **54**(6), 809–834.

Osanov M and **Guest J** (2016) Topology optimization for architected materials design. *Annual Review of Materials Research* **46**(1), 211–233.

Sigmund O (1995) Tailoring materials with prescribed elastic properties. *Mechanics of Materials* **20**(4), 351–368.

Sigmund O (2000) A new class of extremal composites. *Journal of the Mechanics and Physics of Solids* **48**(2), 397–428.

Svanberg K (1987) The method of moving asymptotes–Aa new method for structural optimization. *International Journal for Numerical Methods in Engineering* **24**(2), 359–373.

Thomsen CR, **Wang F** and **Sigmund O** (2018) Buckling strength topology optimization of 2D periodic materials based on linearized bifurcation analysis. *Computer Methods in Applied Mechanics and Engineering* **339**, 115–136.

Torii AJ and **de Faria JR** (2017) Structural optimization considering smallest magnitude eigenvalues: A smooth approximation. *Journal of the Brazilian Society of Mechanical Sciences and Engineering* **39**(5), 1745–1754.

Triantafyllidis N and **Schnaidt WC** (1993) Comparison of microscopic and macroscopic instabilities in a class of two-dimensional periodic composites. *Journal of the Mechanics and Physics of Solids* **41**(9), 1533–1565.

Wang F, **Brøns M** and **Sigmund O** (2023) Non-Hierarchical Architected Materials with Extreme Stiffness and Strength. *Advanced Functional Materials*, 2211561.

Wang F, **Lazarov BS** and **Sigmund O** (2011) On projection methods, convergence and robust formulations in topology optimization. *Structural and Multidisciplinary Optimization* **43**(6), 767–784.

Wang F and **Sigmund O** (2021) 3D architected isotropic materials with tunable stiffness and buckling strength. *Journal of the Mechanics and Physics of Solids* **152**, 104415.

Wilson EL and **Ibrahimbegovic A** (1990) Use of incompatible displacement modes for the calculation of element stiffnesses or stresses. *Finite Elements in Analysis and Design* **7**(3), 229–241.

Wilson EL, **Taylor RL**, **Doherty WP** and **Ghaboussi J** (1973) Incompatible displacement models. In Fenves SJ, Perrone N, Robinson AR and Schnobrich WC (eds), *Numerical and Computer Methods in Structural Mechanics*. Amsterdam: Elsevier, pp. 43–57.

Zheng X, **Smith W**, **Jackson J**, **Moran B**, **Cui H**, **Chen D**, **Ye J**, **Fang N**, **Rodriguez N** and **Weisgraber T** (2016) Multiscale metallic metamaterials. *Nature Materials* **15**(10), 1100.

Cite this article: Wang, F., and Sigmund, O. (2023). Architecting materials for extremal stiffness, yield, and buckling strength. *Programmable Materials*, **1**, e6, https://doi.org/10.1017/pma.2023.5